SUBMITOCHONDRIAL PROTEIN TRANSLOCATION UPON STRESS INHIBITS THERMOGENIC ENERGY EXPENDITURE

Fahrettin Haczeyni[1], Sandra Steensels[1], Benjamin D. Stein[2], James M. Jordan[1], Le Li[3], Vincent Dartigue[1], Selenay S. Sarklioglu[1], Jixuan Qiao[1], Xi K. Zhou[4], Andrew J. Dannenberg[2,#], Neil M. Iyengar[5,6], Haiyuan Yu[3,7], Lewis C. Cantley[2,8] and Baran A. Ersoy[1*]

[1]Division of Gastroenterology and Hepatology, Weill Center for Metabolic Health, Joan & Sanford I. Weill Department of Medicine, Weill Cornell Medicine; New York, NY 10021, USA
[2]Sandra and Edward Meyer Cancer Center, Joan & Sanford I. Weill Department of Medicine, Weill Cornell Medicine; New York, NY 10065, USA
[3]Weill Institute for Cell and Molecular Biology and Department of Computational Biology, Cornell University; Ithaca, NY 14853, USA
[4]Division of Biostatistics, Department of Population Health Sciences, Weill Cornell Medicine; New York, NY 10065, USA
[5]Breast Medicine Service, Memorial Sloan Kettering Cancer Center; New York, NY 10065, USA
[6]Weill Cornell Medical Center; New York, NY 10065, USA
[7]Center for Innovative Proteomics, Cornell University; Ithaca, NY 14853, USA
[8]Dana Farber Cancer Institute, Harvard Medical School; Boston, MA 02215, USA
[#]This author is now retired.

[*]Corresponding Author. Email: bersoy@med.cornell.edu.

Abstract

Mitochondria-rich brown adipocytes dissipate cellular fuel as heat by thermogenic energy expenditure (TEE). Prolonged nutrient excess or cold exposure impair TEE and contribute to the pathogenesis of obesity, but the mechanisms remain incompletely understood. Here we report that stress-induced proton leak into the matrix interface of mitochondrial innermembrane (IM) mobilizes a group of proteins from IM into matrix, which in turn alter mitochondrial bioenergetics. We further determine a smaller subset that correlates with obesity in human subcutaneous adipose tissue. We go on to show that the top factor on this short list, acyl-CoA thioesterase 9 (ACOT9), migrates from the IM into the matrix upon stress where it enzymatically deactivates and prevents the utilization of acetyl-CoA in TEE. The loss of ACOT9 protects mice against the complications of obesity by maintaining unobstructed TEE. Overall, our results introduce aberrant protein translocation as a strategy to identify pathogenic factors.

One-Sentence Summary

Thermogenic stress impairs mitochondrial energy utilization by forcing translocation of IM-bound proteins into the matrix.

In energy homeostasis, white adipose tissue (WAT) stores energy for future use, whereas brown adipose tissue (BAT) consumes energy for the maintenance of body temperature (*1-3*). Hence, thermogenesis in BAT provides a metabolic sink for the catabolic clearance of excess lipids and glucose following activation by food intake and cold exposure (*4-7*). However, thermogenic energy expenditure (TEE) becomes suppressed by chronic nutritional excess and extended periods of cold (*8-10*). This contributes to the pathogenesis of obesity and secondary metabolic complications such as type 2 diabetes, nonalcoholic fatty liver disease, and cardiovascular complications (*11-13*). The identification of pathways that limit TEE should therefore provide strategies for pharmacotherapy against obesity and metabolic comorbidities.

Thermogenesis occurs at the innermembrane (IM) of BAT mitochondria, where the proton gradient established by the breakdown of lipids and glucose becomes uncoupled from oxidative phosphorylation and dissipates chemical energy as heat (*14*). However, chronic stress resulting from nutrient overload or prolonged thermogenic activity leads to reduced IM potential ($\Delta\Psi$) due to increased proton leak from the intermembrane space into the matrix (*15, 16*). The concomitant drop in local pH can influence protein-protein interactions of IM-associated soluble proteins, which can alter their submitochondrial localization and downstream signaling (*17*). For instance, Sirtuin 3 (SIRT3) dissociates from ATP synthase following reduced $\Delta\Psi$ and translocates into the matrix. The subsequent deacetylation of a group of mitochondrial proteins by SIRT3 reorganizes mitochondrial metabolism (*18*). Based on this principle, we postulated that hyperactive thermogenic uncoupling would cause a seismic shift in pH at the matrix interface of IM. Accordingly, we sought to determine the subset of proteins that translocate from IM into matrix in response to extended cold and/or caloric stress using proteomic analysis of BAT submitochondrial fractions. For disease association, we further narrowed down this subset by cross-referencing them to obesity-associated genes in human subcutaneous adipose tissue. Ultimately, we identified a novel biological pathway whereby chronic stress-induced matrix localization of an enzyme called acyl-CoA thioesterase 9 (ACOT9) blocks excess energy utilization in thermogenesis and thereby promotes obesity and metabolic disorders.

Results

To promote a stress response in BAT mitochondria, we subjected mice to caloric stress by feeding a high fat diet (HFD; kcal 20% protein, 20% carb, 60% fat) *ad libitum* for 10 weeks, as opposed to regular diet (RD; kcal 25% protein, 62% carb, 13% fat) as control. After 10 weeks, we applied chronic cold stress by housing at 4°C for 2 weeks, or thermoneutral housing at 30°C for control, which suppresses the drive for thermogenesis (Fig. 1A). Matrix vs. IM occupancy of proteins was determined by mass spectrometry analysis of matrix and IM fractions that were purified from crude BAT mitochondria. Subjecting mice to either or both chronic stress conditions led to striking differences in the IM-to-matrix localization of specific proteins (Fig. 1B). Unsupervised hierarchical clustering of matrix:IM-abundance ratios revealed five clusters. As anticipated, the four largest clusters belonged to proteins that became enriched within the matrix compartment whereas only a small cluster (cluster 1) exhibited reduced matrix abundance in response to HFD and/or cold (Fig. 1B). To more rigorously identify proteins with altered localization in stressed mitochondria, we tested for differential abundance (adjusted $P<0.05$) between matrix and IM fractions within each stress condition. In the non-stressed control group without caloric or thermogenic stress, we found 84 proteins that were significantly more abundant in the matrix relative to IM (adjusted $P<0.05$). Excluding these 84 proteins, we identified an

additional 116, 132, and 140 differentially abundant matrix-localized proteins due to caloric stress, cold stress, or combined stress conditions, respectively (Fig. 1C). Because both caloric and thermogenic stress exacerbate proton leak into mitochondrial matrix (*19*), we overlapped these stress-responsive factors to determine whether reduced $\Delta\Psi$ via different types of stress would trigger the same factors to translocate from IM into matrix. Our analysis showed that nearly half of matrix localizations (121 in 224 proteins) were common in multiple stress conditions (Fig. 1D). Collectively, these stress-responsive proteins, which translocated from IM to matrix were associated with binding, catabolic and anabolic activities, as well as oxidative phosphorylation as evidenced by gene set enrichment analysis (Fig. 1E).

To establish the pathophysiological relevance of these findings to human disease, we conducted an independent transcriptomics analysis of human subcutaneous adipose tissues to identify obesity-associated genes. We found 1013 mitochondrial transcripts (non-mitochondrial genes were filtered out using MitoCarta3.0), of which 131 were significantly positively correlated with increasing body mass index (BMI; range: 17.5-60) (Fig. 1F,G). Overall, among the 121 matrix-localizing common stress-responsive proteins that were identified by the proteomics study, we found 16 mitochondrial factors to be highly associated with obesity in humans (Fig. 1H; fig. S1). On this short list, the top hit was ACOT9 as evidenced by the tightest correlation with increased BMI in humans (Spearman's rho=0.62). ACOT9 is a mitochondrial enzyme that hydrolyzes acetyl coenzyme A (CoA) into unbound (inactive) acetate (*20*). Considering that acetyl-CoA is the common breakdown end-product of nearly all energy sources (*21*), these results suggest that chronic stress-induced translocation of ACOT9 from the IM into the matrix represents a rate-limiting step that blocks acetyl-CoA flux into the tricarboxylic acid (TCA) cycle, thereby limiting TEE.

Because the enzymatic activity of ACOT9 represents a key checkpoint for the majority of mitochondrial catabolic reactions, we sought to further elucidate ACOT9's biological function in the context of thermogenic and caloric stress. We first confirmed that ACOT9 was more abundant in the IM than the matrix of BAT mitochondria in the absence of any stress, but translocated into the matrix upon caloric stress and/or chronic cold (Fig. 2A; fig. S2). To address whether the translocation of ACOT9 from IM into matrix followed a pH-dependent mechanism as seen with SIRT3 (*18*), we scanned proteome-wide interactome studies to find ACOT9-binding partners at the IM (*22*). Among experimentally-established ACOT9-interacting proteins, the electron transport chain (ETC) Complex I subunit NADH:Ubiquinone oxidoreductase core subunit S7 (NDUFS7) was the only mitochondrial binding partner (fig. S3). In pulldown assays, ACOT9 interacted with NDUFS7 at resting mitochondrial pH of 7.4 underlying its localization to the IM in the absence of mitochondrial stress (Fig. 2B). *In silico* prediction modeling for the ACOT9-NDUFS7 complex revealed two Histidine residues (ACOT9 His385 and NDUFS7 His95) within the interaction interface (Fig. 2C; fig. S4). Because Histidine is the only amino acid that becomes protonated upon a pH drop from 7.4 to 6.0 (*23*), we tested the impact of low pH on ACOT9 interactions with NDUFS7. We found that ACOT9 failed to pulldown NDUFS7 when the assay buffer condition was lowered from pH 7.4 to 6.0 to simulate proton leak in low $\Delta\Psi$ (Fig. 2D). In addition, fractionation of submitochondrial compartments using a low pH buffer of 6.0 resulted in the accumulation of most ACOT9 protein within the matrix compartment regardless of stress, while another peripheral soluble protein, cytochrome C, remained present at the IM compartment as control (Fig. 2E). The influence of pH on ACOT9-NDUFS7 interactions was also confirmed by performing an *in situ* proximity ligation assay in cultured cells, in which promoting proton leak with an ionophore (FCCP; carbonyl cyanide-p-trifluoromethoxyphenylhydrazone) ablated the

interactions (Fig. 2F). Taken together, these findings demonstrate a pH-dependent mechanism by which rate-limiting enzymes such as ACOT9 can be regulated (Fig. 2G).

We have previously shown that ACOT9 within the liver promotes glucose production and *de novo* lipogenesis by increasing the anabolic flux through the TCA cycle (*24*). Independent of its hepatic function, *Acot9*$^{-/-}$ mice also exhibited increased EE and reduced adiposity when fed HFD. Because the liver-specific loss of ACOT9 did not improve EE and adiposity, the mechanisms by which extrahepatic ACOT9 expression suppressed EE remained unexplored. To test the role of ACOT9 in BAT, we ramped down the ambient temperature of mice from thermoneutrality to room temperature and then to cold exposure, which gradually increased the biological demand for TEE (fig. S5). Indirect calorimetry measurements indicated that the maximal oxygen consumption (VO_2) and EE of *Acot9*$^{-/-}$ mice diverged from wildtype (*WT*) littermates (*Acot9*$^{+/+}$) as the demand for TEE increased. Moreover, *Acot9*$^{-/-}$ mice maintained their core body temperature even after two weeks of mild cold exposure (10°C) unlike *WT* counterparts (fig. S6). To determine whether increased EE in *Acot9*$^{-/-}$ mice was due to BAT activity and not another futile mechanism (*25*), TEE was specifically activated by injecting mice with the β_3 adrenergic receptor (β_3-AR) agonist CL-316,243. We found that *Acot9*$^{-/-}$ mice VO_2 rates were markedly higher than *WT* regardless of the diet upon BAT activation (Fig. 3A). On the other hand, physical activity (fig. S7A) and digestive efficacy (fig. S7B) did not contribute to the altered energy homeostasis between *Acot9*$^{-/-}$ and *WT* mice. Because BAT is the main hub for TEE, we studied the impact of ACOT9 in BAT by generating mice with BAT-specific ablation of ACOT9 (*Acot9*$^{B\text{-}KO}$) (fig. S8A). In a trend similar to *Acot9*$^{-/-}$ mice (*24*), *Acot9*$^{B\text{-}KO}$ mice gained 13% less body weight compared to *Acot9*$^{B\text{-}WT}$ littermates after 10 weeks on HFD (Fig. 3B), which was attributable to 43% weight reduction in total fat mass (Fig. 3C). Unlike fat mass, lean mass remained unchanged in these mouse lines (fig. S8B,C). Despite reduced adiposity, *Acot9*$^{B\text{-}KO}$ mice consumed 10% more food than *Acot9*$^{B\text{-}WT}$ under thermogenic conditions (Fig. 3D). The compensatory aspect of increased food intake was supported by *Acot9*$^{B\text{-}KO}$ mice losing 30% more weight than *Acot9*$^{B\text{-}WT}$ following a 6-hour fast when they were unable to make up for increased TEE by eating more (Fig. 3E). Indirect calorimetry analysis of *Acot9*$^{B\text{-}KO}$ mice indicated that the loss of ACOT9 expression in BAT alone was sufficient to increase VO_2, VCO_2, and EE compared to *Acot9*$^{B\text{-}WT}$ counterparts (Fig. 3F,G; fig. S9). During the indirect calorimetry analysis, food intake remained higher for *Acot9*$^{B\text{-}KO}$ mice compared to *Acot9*$^{B\text{-}WT}$ littermates (Fig. 3H), but there was no significant difference in physical activity (fig. S9).

To elucidate the significance of ACOT9's enzymatic activity in BAT, we first confirmed that the deletion of ACOT9 in BAT did not alter the expression of other ACOT family members (fig. S10A). We next verified that the thioesterase activity of ACOT9 in BAT is specifically directed toward the hydrolysis of short-chain acyl-CoA such as acetyl-CoA (2C), propionyl-CoA (3C), and butyryl-CoA (4C), but not mid- or long-chain acyl-CoA species (Fig. 3I). Considering that propionyl-CoA is the breakdown end-product of odd-chain acyl-CoA, which represent less than 1% of acyl-CoA, and that butyryl-CoA is further oxidized into acetyl-CoA, these results solidify the role of ACOT9 as a key checkpoint for acetyl-CoA flux into the TCA cycle. Mass spectrometry-based metabolomics analysis of BATs further supported the role of ACOT9 in limiting the utilization of acetyl-CoA in pathways essential to thermogenesis, including TCA cycle, pyruvate and butyrate metabolisms, ETC, nicotinate and nicotinamide metabolisms, fatty acid (FA) oxidation, glycerolipid metabolism, *de novo* lipogenesis, and cardiolipin biosynthesis (Fig 3J). Among BAT metabolites, acetyl-CoA, nicotinamide adenine dinucleotide (NADH), NAD(P)H, glutathione/oxidized GSH (GSSG), and glycerol-3-phosphate abundance trended

higher, whereas ATP:AMP and pyruvate levels were lower in *Acot9*$^{B\text{-}KO}$ mouse BATs compared to *Acot9*$^{B\text{-}WT}$ counterparts (Fig. 3K).

Because TEE is primarily fueled by β-oxidation following lipolysis, we assessed basal and isoproterenol-stimulated lipolysis rates in *Acot9*$^{-/-}$ and *WT* primary BAT cultures. In further support of improved FA utilization and disposal, the loss of ACOT9 increased overall lipolysis levels (Fig. 4A). Nonetheless, increased thermogenesis was not additionally supplemented by enhanced WAT lipolysis as evidenced by a lack of difference in *ex situ* lipolysis of WAT (fig. S11). ACOT9 also inhibited β-oxidation as evidenced by decreased basal and norepinephrine (NE)-stimulated oxygen consumption rates (Fig. 4B), as well as breakdown of radiolabeled (^{14}C)-palmitate in complementary assays (Fig. 4C). Although the rates of FA uptake (fig. S12A), *de novo* lipogenesis (fig. S12B), and overall lipid accumulation (fig. S12C) remained unchanged, mRNA abundance for fatty acid translocase (CD36) and carnitine palmitoyltransferase 1 (CPT1) were higher in *Acot9*$^{B\text{-}KO}$ mice BATs vs. *Acot9*$^{B\text{-}WT}$ counterparts (fig. S10B). Lipidomics analysis indicated that ACOT9 promoted the accumulation of saturated triglyceride species (fig. S13A,B). Overall, these findings emphasize the significance of ACOT9 as a key checkpoint in FA utilization in BAT.

β-oxidation of lipids is not the sole type of fuel for BAT TEE. An increasing number of studies have established glucose as a substantial cellular fuel that feeds TEE through intermediary mechanisms in BAT (*19, 26-28*). Noticeably, both HFD-fed *Acot9*$^{B\text{-}KO}$ (Fig. 4D) and *Acot9*$^{-/-}$ (fig. S14) mice exhibited higher utilization of carbohydrates as fuel, which was evidenced by increased respiratory exchange ratio (RER). We therefore assessed glucose tolerance in weight-matched *Acot9*$^{B\text{-}KO}$ mice and *Acot9*$^{B\text{-}WT}$ littermates (Fig. 4E). BAT-specific ablation of ACOT9 resulted in 25% faster glucose disposal in HFD-fed mice without altering fasting blood glucose. To determine whether this difference was due to glucose clearance via BAT thermogenic activity, we tested glucose-induced thermogenesis using intrascapular thermal imaging (*29*). A bolus dose of glucose injection increased heat dissipation in dorsal area of *Acot9*$^{B\text{-}KO}$ mice by 0.9°C higher than *Acot9*$^{B\text{-}WT}$ littermates (Fig. 4F), while core body temperature remained stable (fig. S15). In line with these findings, the deletion of ACOT9 accelerated BAT glycolytic metabolism as evidenced by upregulation of key glycolysis enzymes such as hexokinase (HK) I, HK II, pyruvate dehydrogenase (PD), and pyruvate kinase 1/2 (PKM1/2) in *Acot9*$^{B\text{-}KO}$ mice BATs vs. *Acot9*$^{B\text{-}WT}$ counterparts (Fig. 4G). Likewise, uncoupling protein 1 (UCP1), the enzyme central to the thermogenic activity also showed higher expression levels in BAT of *Acot9*$^{B\text{-}KO}$ mice than *Acot9*$^{B\text{-}WT}$ littermates (Fig. 4G). In further support of improved glucose utilization, we found that primary brown adipocytes lacking ACOT9 exhibited significant increases in both glucose uptake and extracellular acidification rate (ECAR) despite the high insulin concentration in the culture maintenance media (Figs. 4H and 4I). These data support the notion that BAT cells upregulate pathways to break down glucose into acetyl-CoA and dissipate it as heat in the absence of an active ACOT9 within the matrix.

Discussion

Recent studies on mitochondrial structural and functional proteomics have outlined how remarkably complex the mitochondrial protein landscape is (*30-32*). Comprising nearly 1,500 proteins in humans, mitochondria execute an important number of diverse functions; however, the sublocalization of mitochondrial protein subsets, especially in mitochondrial dysfunction remain poorly recognized. Our results provide mechanistic evidence that matrix-soluble enzymes are dynamic factors in terms of their submitochondrial localization and can migrate upon stress stimuli

within mitochondria to catalyze their specific reactions. The most important finding in the present study is that excessive proton accumulation at the matrix interface of IM that is resultant to metabolic stressors can lead to weakened protein-protein interactions and cause translocation of an IM-bound protein into the matrix. The data thus introduce a new paradigm that concerns overall metabolic health through the scope of a new mitochondrial stress response. Nonetheless, it should be noted that the current studies have been conducted in the context of UCP1-dependent thermogenesis, and other futile cycles such as creatine kinase and sarcolipin activity as well as triglyceride cycling may function independently from proton flux-induced protein translocation (*33, 34*).

While our multiomics analyses pointed to a subset of metabolic proteins that included SIRT and ACOT family members, we expanded our findings concerning ACOT9 for two main reasons: Firstly, ACOT9 is the primary checkpoint for acetyl-CoA utilization in TCA cycle that is central to energy homeostasis. Secondly, of the mitochondrial proteins, ACOT9 had the strongest association with obesity in humans. Our data suggest that the submitochondrial localization of an enzyme might be important for two main reasons: i. the enzyme might be dormant or active while docked at the IM, or ii. the enzyme might be restrained and away from its specific substrate(s). Our extension of this concept to ACOT9 indicates that ACOT9 lays dormant while in interaction with NDUFS7 as monomeric ACOTs are catalytically inactive (*20, 35*). Thus, its dissociation from NDUFS7 would not only give way to its activation by multimerization but also expose it to its substrate acetyl-CoA within the matrix. Likely evolved and conserved to prevent uncontrolled energy loss via thermogenesis, our results indicate that ACOT9 promotes obesity and related metabolic disorders given the current epidemic of excessive calorie consumption. Targeted inhibition of ACOT9 might increase energy expenditure and thereby be useful in the treatment of metabolic disorders.

Histidine protonation can promote the disassociation of proteins from the IM by two primary mechanisms: the first of which is playing a pivotal role in protein-protein interactions within the binding domain as in ACOT9 and NDUFS7. Secondly, Histidine residues on a protein would translate to a higher net charge at low pH, which can alter the structural homogeneity and stability of the whole protein (*23, 36*). Interestingly, a recent study has shown that the ETC complex II components disassemble in response to macrophage inflammatory activation (*37*), a phenomenon which is also supported by our finding of ETC components within the matrix fraction under stress conditions. Whether the IM-to-matrix translocation of proteins other than ACOT9 also depends on Histidine protonation will require determining the role of these residues within each translocating protein in their structure and protein interactions.

In the current study, we took advantage of BAT's unique physiology to observe maximal proton surge from the intermembrane space into the matrix in the setting of health and disease, which has clear implications for the treatment of metabolic disorders. Needless to say that mitochondrial stress and dysfunction are detrimental for a wider array of disorders including but not limited to developmental, neurological, cardiovascular, and metabolic problems as well as immunodeficiency and cancer (*38, 39*). In this context, submitochondrial protein translocation as a mitochondrial stress response has the potential to have wider implications in health and future pharmacotherapy research.

References and Notes

1. M. Chondronikola *et al.*, Brown adipose tissue improves whole-body glucose homeostasis and insulin sensitivity in humans. *Diabetes* **63**, 4089-4099 (2014).
2. K. A. Iwen *et al.*, Cold-induced brown adipose tissue activity alters plasma fatty acids and improves glucose metabolism in men. *The Journal of Clinical Endocrinology & Metabolism* **102**, 4226-4234 (2017).
3. D. G. Sadler, L. Treas, J. D. Sikes, C. Porter, A modest change in housing temperature alters whole body energy expenditure and adipocyte thermogenic capacity in mice. *American Journal of Physiology-Endocrinology and Metabolism* **323**, E517-E528 (2022).
4. Y. Schutz, T. Bessard, E. Jequier, Diet-induced thermogenesis measured over a whole day in obese and nonobese women. *The American journal of clinical nutrition* **40**, 542-552 (1984).
5. A. M. Cypess *et al.*, Identification and importance of brown adipose tissue in adult humans. *New England journal of medicine* **360**, 1509-1517 (2009).
6. T. Yoneshiro *et al.*, Brown adipose tissue, whole-body energy expenditure, and thermogenesis in healthy adult men. *Obesity* **19**, 13-16 (2011).
7. C. Hepler *et al.*, Time-restricted feeding mitigates obesity through adipocyte thermogenesis. *Science* **378**, 276-284 (2022).
8. S. L. Wijers, W. H. Saris, W. D. van Marken Lichtenbelt, Individual thermogenic responses to mild cold and overfeeding are closely related. *The Journal of Clinical Endocrinology & Metabolism* **92**, 4299-4305 (2007).
9. G. H. Vijgen *et al.*, Brown adipose tissue in morbidly obese subjects. *PloS one* **6**, e17247 (2011).
10. D. A. Giles *et al.*, Thermoneutral housing exacerbates nonalcoholic fatty liver disease in mice and allows for sex-independent disease modeling. *Nature medicine* **23**, 829-838 (2017).
11. X. Yang, S. Enerbäck, U. Smith, Reduced expression of FOXC2 and brown adipogenic genes in human subjects with insulin resistance. *Obesity research* **11**, 1182-1191 (2003).
12. L. Poekes *et al.*, Defective adaptive thermogenesis contributes to metabolic syndrome and liver steatosis in obese mice. *Clinical Science* **131**, 285-296 (2017).
13. T. Becher *et al.*, Brown adipose tissue is associated with cardiometabolic health. *Nature medicine* **27**, 58-65 (2021).
14. M. A. Ballinger, M. T. Andrews, Nature's fat-burning machine: brown adipose tissue in a hibernating mammal. *The Journal of experimental biology* **221**, (2018).
15. A. Rupprecht *et al.*, Role of the transmembrane potential in the membrane proton leak. *Biophysical Journal* **98**, 1503-1511 (2010).
16. M. Liesa, O. S. Shirihai, Mitochondrial dynamics in the regulation of nutrient utilization and energy expenditure. *Cell metabolism* **17**, 491-506 (2013).
17. A. B. Schendzielorz *et al.*, Two distinct membrane potential–dependent steps drive mitochondrial matrix protein translocation. *Journal of Cell Biology* **216**, 83-92 (2017).
18. W. Yang *et al.*, Mitochondrial sirtuin network reveals dynamic SIRT3-dependent deacetylation in response to membrane depolarization. *Cell* **167**, 985-1000. e1021 (2016).
19. B. Cannon, J. Nedergaard, Brown adipose tissue: function and physiological significance. *Physiological reviews*, (2004).

20. V. Tillander *et al.*, Acyl-CoA thioesterase 9 (ACOT9) in mouse may provide a novel link between fatty acid and amino acid metabolism in mitochondria. *Cellular and molecular life sciences* **71**, 933-948 (2014).
21. L. Shi, B. P. Tu, Acetyl-CoA and the regulation of metabolism: mechanisms and consequences. *Current opinion in cell biology* **33**, 125-131 (2015).
22. E. L. Huttlin *et al.*, Architecture of the human interactome defines protein communities and disease networks. *Nature* **545**, 505-509 (2017).
23. S. Li, M. Hong, Protonation, tautomerization, and rotameric structure of histidine: a comprehensive study by magic-angle-spinning solid-state NMR. *Journal of the American Chemical Society* **133**, 1534-1544 (2011).
24. S. Steensels *et al.*, Acyl-Coenzyme A Thioesterase 9 Traffics Mitochondrial Short-Chain Fatty Acids Toward De Novo Lipogenesis and Glucose Production in the Liver. *Hepatology* **72**, 857-872 (2020).
25. K. Ikeda *et al.*, UCP1-independent signaling involving SERCA2b-mediated calcium cycling regulates beige fat thermogenesis and systemic glucose homeostasis. *Nature medicine* **23**, 1454-1465 (2017).
26. W. D. van Marken Lichtenbelt *et al.*, Cold-activated brown adipose tissue in healthy men. *New England Journal of Medicine* **360**, 1500-1508 (2009).
27. M. K. Hankir, M. Klingenspor, Brown adipocyte glucose metabolism: a heated subject. *EMBO reports* **19**, e46404 (2018).
28. S. M. Jung *et al.*, In vivo isotope tracing reveals the versatility of glucose as a brown adipose tissue substrate. *Cell reports* **36**, 109459 (2021).
29. J. D. Crane, E. P. Mottillo, T. H. Farncombe, K. M. Morrison, G. R. Steinberg, A standardized infrared imaging technique that specifically detects UCP1-mediated thermogenesis in vivo. *Molecular metabolism* **3**, 490-494 (2014).
30. V. Hung *et al.*, Proteomic mapping of the human mitochondrial intermembrane space in live cells via ratiometric APEX tagging. *Molecular cell* **55**, 332-341 (2014).
31. F.-N. Vögtle *et al.*, Landscape of submitochondrial protein distribution. *Nature communications* **8**, 290 (2017).
32. N. Pfanner, B. Warscheid, N. Wiedemann, Mitochondrial proteins: from biogenesis to functional networks. *Nature Reviews Molecular Cell Biology* **20**, 267-284 (2019).
33. L. Kazak *et al.*, A creatine-driven substrate cycle enhances energy expenditure and thermogenesis in beige fat. *Cell* **163**, 643-655 (2015).
34. J. F. Rahbani *et al.*, Creatine kinase B controls futile creatine cycling in thermogenic fat. *Nature* **590**, 480-485 (2021).
35. V. Tillander, S. E. Alexson, D. E. Cohen, Deactivating fatty acids: acyl-CoA thioesterase-mediated control of lipid metabolism. *Trends in Endocrinology & Metabolism* **28**, 473-484 (2017).
36. A. G. Rao, C. Wiebeler, S. Sen, D. S. Cerutti, I. Schapiro, Histidine protonation controls structural heterogeneity in the cyanobacteriochrome AnPixJg2. *Physical Chemistry Chemical Physics* **23**, 7359-7367 (2021).
37. M. B. Reynolds *et al.*, Cardiolipin coordinates inflammatory metabolic reprogramming through regulation of Complex II disassembly and degradation. *Science Advances* **9**, eade8701 (2023).
38. H. T. Langer, L. C. Cantley, M. D. Goncalves, Live cold to grow old? Thermogenesis to fight cancer. *Cell Research*, 1-2 (2022).

39. T. Seki *et al.*, Brown-fat-mediated tumour suppression by cold-altered global metabolism. *Nature* **608**, 421-428 (2022).
40. B. A. Cho *et al.*, Blood biomarkers reflect the effects of obesity and inflammation on the human breast transcriptome. *Carcinogenesis* **42**, 1281-1292 (2021).
41. A. Dobin *et al.*, STAR: ultrafast universal RNA-seq aligner. *Bioinformatics* **29**, 15-21 (2013).
42. S. Anders, P. T. Pyl, W. Huber, HTSeq—a Python framework to work with high-throughput sequencing data. *bioinformatics* **31**, 166-169 (2015).
43. L. He, J. Diedrich, Y.-Y. Chu, J. R. Yates III, Extracting accurate precursor information for tandem mass spectra by RawConverter. *Analytical chemistry* **87**, 11361-11367 (2015).
44. T. Xu *et al.*, ProLuCID: An improved SEQUEST-like algorithm with enhanced sensitivity and specificity. *Journal of proteomics* **129**, 16-24 (2015).
45. M. D. Goncalves *et al.*, Fenofibrate prevents skeletal muscle loss in mice with lung cancer. *Proceedings of the National Academy of Sciences* **115**, E743-E752 (2018).
46. Y. Satomi, M. Hirayama, H. Kobayashi, One-step lipid extraction for plasma lipidomics analysis by liquid chromatography mass spectrometry. *Journal of Chromatography B* **1063**, 93-100 (2017).
47. H. Tsugawa *et al.*, MS-DIAL: data-independent MS/MS deconvolution for comprehensive metabolome analysis. *Nature methods* **12**, 523-526 (2015).
48. A. I. Mina *et al.*, CalR: a web-based analysis tool for indirect calorimetry experiments. *Cell metabolism* **28**, 656-666. e651 (2018).
49. A. Staffas *et al.*, Nutritional support from the intestinal microbiota improves hematopoietic reconstitution after bone marrow transplantation in mice. *Cell host & microbe* **23**, 447-457. e444 (2018).
50. F. Pallotti, G. Lenaz, Isolation and subfractionation of mitochondria from animal cells and tissue culture lines. *Methods in cell biology* **65**, 1-35 (2001).
51. K. Okada *et al.*, Thioesterase superfamily member 1 suppresses cold thermogenesis by limiting the oxidation of lipid droplet-derived fatty acids in brown adipose tissue. *Molecular metabolism* **5**, 340-351 (2016).
52. Z. Pei *et al.*, Mouse very long-chain Acyl-CoA synthetase 3/fatty acid transport protein 3 catalyzes fatty acid activation but not fatty acid transport in MA-10 cells. *Journal of Biological Chemistry* **279**, 54454-54462 (2004).
53. K. Kanno *et al.*, Interacting proteins dictate function of the minimal START domain phosphatidylcholine transfer protein/StarD2. *Journal of Biological Chemistry* **282**, 30728-30736 (2007).
54. R. Evans *et al.*, Protein complex prediction with AlphaFold-Multimer. *BioRxiv*, 2021.2010.2004.463034 (2021).
55. B. Zhong *et al.*, in *International Conference on High Performance Computing in Asia-Pacific Region Workshops*. (2022), pp. 1-9.
56. V. Mariani, M. Biasini, A. Barbato, T. Schwede, lDDT: a local superposition-free score for comparing protein structures and models using distance difference tests. *Bioinformatics* **29**, 2722-2728 (2013).
57. A. Vandenbon, Evaluation of critical data processing steps for reliable prediction of gene co-expression from large collections of RNA-seq data. *Plos one* **17**, e0263344 (2022).

58. Z. Pang *et al.*, Using MetaboAnalyst 5.0 for LC–HRMS spectra processing, multi-omics integration and covariate adjustment of global metabolomics data. *Nature Protocols* **17**, 1735-1761 (2022).
59. R. Guo, S. Zong, M. Wu, J. Gu, M. Yang, Architecture of human mitochondrial respiratory megacomplex I2III2IV2. *Cell* **170**, 1247-1257. e1212 (2017).
60. Z. Gu, R. Eils, M. Schlesner, Complex heatmaps reveal patterns and correlations in multidimensional genomic data. *Bioinformatics* **32**, 2847-2849 (2016).
61. M. E. Ritchie *et al.*, limma powers differential expression analyses for RNA-sequencing and microarray studies. *Nucleic acids research* **43**, e47-e47 (2015).
62. L. E. Goeminne, K. Gevaert, L. Clement, Peptide-level robust ridge regression improves estimation, sensitivity, and specificity in data-dependent quantitative label-free shotgun proteomics. *Molecular & Cellular Proteomics* **15**, 657-668 (2016).
63. G. R. Warnes *et al.*, gplots: Various R programming tools for plotting data. *R package version* **2**, 1 (2009).

Acknowledgments

We thank Geoffrey C. Farrell (The Australian National University, Australia), Isabelle A. Leclercq (Université Catholique de Louvain, Belgium), and Paul Cohen (The Rockefeller University, USA) for insightful comments on the manuscript. We also thank David E. Cohen (Brigham and Women's Hospital, Harvard University, USA) and his laboratory members for helpful discussions. We thank Timothy E. McGraw (WCM) for providing the *Ucp1-Cre* mouse, and Veronika Tillander and Stefan E. H. Alexson (Karolinska Institutet, Sweden) for providing the recombinant ACOT9 plasmid construct. We thank Frederick R. Maxfield and Timothy A. Ryan (WCM) for their expert advice on the biochemistry of protein-protein interaction. Finally, we thank Weill Cornell Medicine Metabolic Phenotyping Core, Proteomics and Metabolomics Core, and Research Animal Resource Center for excellent assistance with experiments.

Funding

This study was financially supported, in part, by;

- National Institutes of Health (NIH) R01 DK129576 grant to BAE; P01 CA120964 and R35 CA197588 to LCC; R01 GM124559, R01 GM125639 and R01 DK115398 to HY; T32DK116970-04 Ruth L. Kirschstein T32 Research Award to JMJ.
- Weill Cornell Medicine Institutional Fund and Seed Grant for Innovative Ideas to BAE.
- Simons Foundation grants 575547 and 893926 to HY.

Author Contributions

FH expanded upon the concept, conceived the experimental plan, designed and performed experiments, analyzed data, and prepared the figures. SS designed and performed experiments, and analyzed data. BDS designed and performed mass spectrometry-based proteomics, and analyzed data. JMJ analyzed proteomics and human transcriptomics data, produced databases, and contributed to figures. LL performed computational modeling of ACOT9-NDUFS7 complex interactions. VD contributed to thermography imaging. JQ produced recombinant protein. SSS performed proximity ligation assay. XKZ contributed to the analysis of the human RNAseq dataset. AJD provided the human RNAseq dataset. NMI collected human samples. HY oversaw computational modeling. LCC oversaw mass spectrometry-based proteomics. BAE conceived the

hypothesis, designed experiments, analyzed data, and directed the project. FH and BAE wrote the manuscript with input from all authors.

Competing Interests

The authors declare that they do not have any competing interests, unless otherwise stated: LCC is the co-founder member of the SAB, and holds equity in Faeth Therapeutics, Volastra Therapeutics, and Larkspur Therapeutics. He is also a co-founder and former member of the SAB and BOD, and holds equity in Agios Pharmaceuticals. AJD is an SAB member of SynDevRx and Health Outlook. NMI has affiliations with the Conquer Cancer Foundation, Novartis, SynDevRx, Pfizer, and Seattle Genetics. These companies have no commercial relationship and do not develop drugs related to the present manuscript.

Data and Materials Availability

All data that support the findings of this study are available in the manuscript or the supplementary materials, and available upon request.

Supplementary Materials

Materials and Methods

Figs. S1 to S15

Fig. 1. Identification of obesity-associated and matrix-translocating mitochondrial proteome. (**A**) Experimental design for BAT submitochondrial proteomics (n=3 mice/condition). (**B**) Unsupervised hierarchical clustering of relative abundances of matrix (Mtx):innermembrane (IM) mitochondrial proteins under different stress conditions. Z-score is scaled Mtx/IM ratio. (**C**) Overlapping set analysis of proteins that are differentially more abundant in the matrix following caloric stress (red, 116), cold stress (blue, 132), and combined stress (purple, 140) conditions compared to matrix-localized proteins in non-stressed control (coral, 84). (**D**) Matrix-localizing proteins that are common in response to multiple stress conditions (green, 121). (**E**) Gene set enrichment analysis of 121 common translocating factors (green in panel D) showing involvement in binding and thermogenic pathways (FDR q-value<0.05) (**F**) Outline of the experimental design for the transcriptomic analysis of BMI-associated (range: 17.5-60) mitochondrial factors in human subcutaneous adipose tissue (Bonferroni-adjusted *P*-value<0.05, Pearson's test, two-sided). (**G**) Top common and mitochondrial obesity-associated factors. (**H**) Obesity-associated mitochondrial factors that overlap with stress-responsive matrix-localizing proteins from panel D (top 3; Bonferroni-adjusted *P*-value<0.05, Pearson's test (blue line), two-sided for R^2>0.2; Spearman's test (red line), Rho>0.5).

Fig. 2. Stress-induced translocation of ACOT9 from IM into matrix is pH-dependent. (**A**) ACOT9 expression in the innermembrane (IM) and Matrix (Mtx) fractions of BAT mitochondria by immunoblot analyses. Inset bar graphs indicate densitometry analyses (data are depicted as mean ± SEM; ****P*<0.001, *****P*<0.0001, independent samples *t*-test). (**B**) Recombinant ACOT9 fused to maltose binding protein (MBP-ACOT9) or MBP alone as negative control were used to pulldown NDUFS7 from HEK293E protein lysate. (**C**) Computational modeling of ACOT9-NDUFS7 interaction with amino acids highlighted in the interaction interface (light gray residues on ACOT9 and yellow residues on NDUFS7). Two Histidine residues in the interaction interface are highlighted blue for ACOT9 H385 and red for NDUFS7 H95. (**D**) Co-pulldown of NDUFS7

with ACOT9 at pH 7.5 vs. 6.0. (**E**) ACOT9 localization in brown adipose submitochondrial fractions in neutral vs. lower pH. (**F**) *In situ* proximity ligation assay (PLA) where Texas Red (peaks at 589/615 nm) indicates ACOT9-NDUFS7 interactions under control or proton-leak that was induced by an ionophore (FCCP). (**G**) Working model of ACOT9 localization behavior in conjunction with ETC Complex I-resident NDUFS7 and reduced pH.

Fig. 3. The loss of ACOT9 protects against adiposity by promoting TEE. (**A**) Oxygen consumption rates (VO_2) of HFD and RD-fed *Acot9*$^{-/-}$ and *WT* mice (n=6) in response to thermogenic stimulation by CL-316,243 injection (1 mg/kg body mass). Bar graphs indicate areas under the VO_2 curves (AUC). (**B** to **H**) Metabolic data from 10 weeks HFD-fed *Acot9*$^{B\text{-}KO}$ and *Acot9*$^{B\text{-}WT}$ mice (n=8). (**B**) Total body weight. (**C**) Total fat mass by EchoMRI. (**D**) Daily food intake under thermogenic condition (4°C). (**E**) Weight loss following 6-hour fast. (**F**) Hourly and (**G**) cumulative energy expenditure (EE) of HFD-fed *Acot9*$^{B\text{-}KO}$ and *Acot9*$^{B\text{-}WT}$ mice (n=5) by indirect calorimetry. (**H**) HFD-fed *Acot9*$^{B\text{-}KO}$ and *Acot9*$^{B\text{-}WT}$ mice (n=5) food intake (kcal) per hour for 3 days period. (**I**) Thioesterase activity in the BAT of HFD-fed *Acot9*$^{-/-}$ and *WT* mice against short- and long-chain fatty acids. (**J**) Metabolic pathway analysis of HFD-fed *Acot9*$^{B\text{-}KO}$ and *Acot9*$^{B\text{-}WT}$ mouse BATs was determined by mass spectrometry-based metabolomics. (**K**) Metabolites that are directly implicated in mitochondrial activity in the BATs of HFD-fed *Acot9*$^{B\text{-}KO}$ and *Acot9*$^{B\text{-}WT}$ mice. Graphs show mean ± SEM. Comparisons in panels A, F and G were adjusted by analysis of covariance (ANCOVA) for corrected body weight ($P<0.05$) with an F-value ($F>3.95$) that shows a significant difference between groups. Comparisons in panels B-E and J were analyzed by independent samples *t*-test (*$P<0.05$, **$P<0.01$). The data in panel H were used by linear regression, from which fitted with Michaelis-Menten Curve (*$P<0.05$, ***$P<0.001$, ****$P<0.0001$).

Fig. 4. BAT-specific deletion of ACOT9 improves excess energy utilization via thermogenesis. (**A** to **C**) Data from cultured *Acot9*$^{-/-}$ and *WT* primary brown adipocytes. (**A**) Lipolysis was determined as a function of released glycerol following stimulation with isoproterenol (1 μM) or dimethyl sulfoxide (DMSO) for vehicle. (**B**) Basal and norepinephrine-stimulated (5 μM final concentration/well) oxygen consumption rates (OCR) as determined by seahorse flux analysis. (**C**) Fatty acid oxidation as determined by the breakdown of ^{14}C-labelled palmitic acid into CO_2 and acid-soluble metabolites. (**D**) Respiratory exchange ratio (RER) of HFD-fed *Acot9*$^{B\text{-}KO}$ and *Acot9*$^{B\text{-}WT}$ mice at thermogenic condition (4°C) (n=8). Bar graphs reflect areas under the RER curves (AUC) during light, dark, and full day. (**E**) Systemic glucose tolerance in HFD-fed *Acot9*$^{B\text{-}KO}$ and *Acot9*$^{B\text{-}WT}$ mice tested by intraperitoneal glucose tolerance test (IpGTT; 2 g/kg body mass) (n=8). Bar graph represents AUC. (**F**) Thermographic analyses of HFD-fed *Acot9*$^{B\text{-}KO}$ and *Acot9*$^{B\text{-}WT}$ mice dorsal area measured at fasting and 30 minutes after glucose injection (2 g/kg body mass) (n=6). (**G**) The relative abundance of proteins that are involved in glycolysis (hexokinase I (HK I), HK II, pyruvate kinase 1/2 (PKM1/2), and pyruvate dehydrogenase (PD)) and thermogenesis (uncoupling protein 1 (UCP1)) in BATs of HFD-fed *Acot9*$^{B\text{-}KO}$ and *Acot9*$^{B\text{-}WT}$ mice was determined by immunoblot analysis. Inset bar graphs indicate densitometry analyses. (**H**) Glucose uptake in cultured *Acot9*$^{-/-}$ and *WT* primary brown adipocytes. (**I**) Basal and norepinephrine-stimulated (5 μM final concentration/well) extracellular acidification rates (ECAR) of cultured *Acot9*$^{-/-}$ and *WT* primary brown adipocytes. Graphs show mean ± SEM. Comparisons in panels A, B, E, and I were analyzed by two-way analysis of variance (ANOVA) with Bonferroni's *post hoc* correction (*$P<0.05$, **$P<0.01$, ***$P<0.001$, ****$P<0.0001$).

Comparisons in panels C, D, G and H were analyzed by independent samples *t*-test (**P*<0.05, ***P*<0.01). The data at panel F were analyzed by linear regression *t*-test on the slope (****P*<0.001).

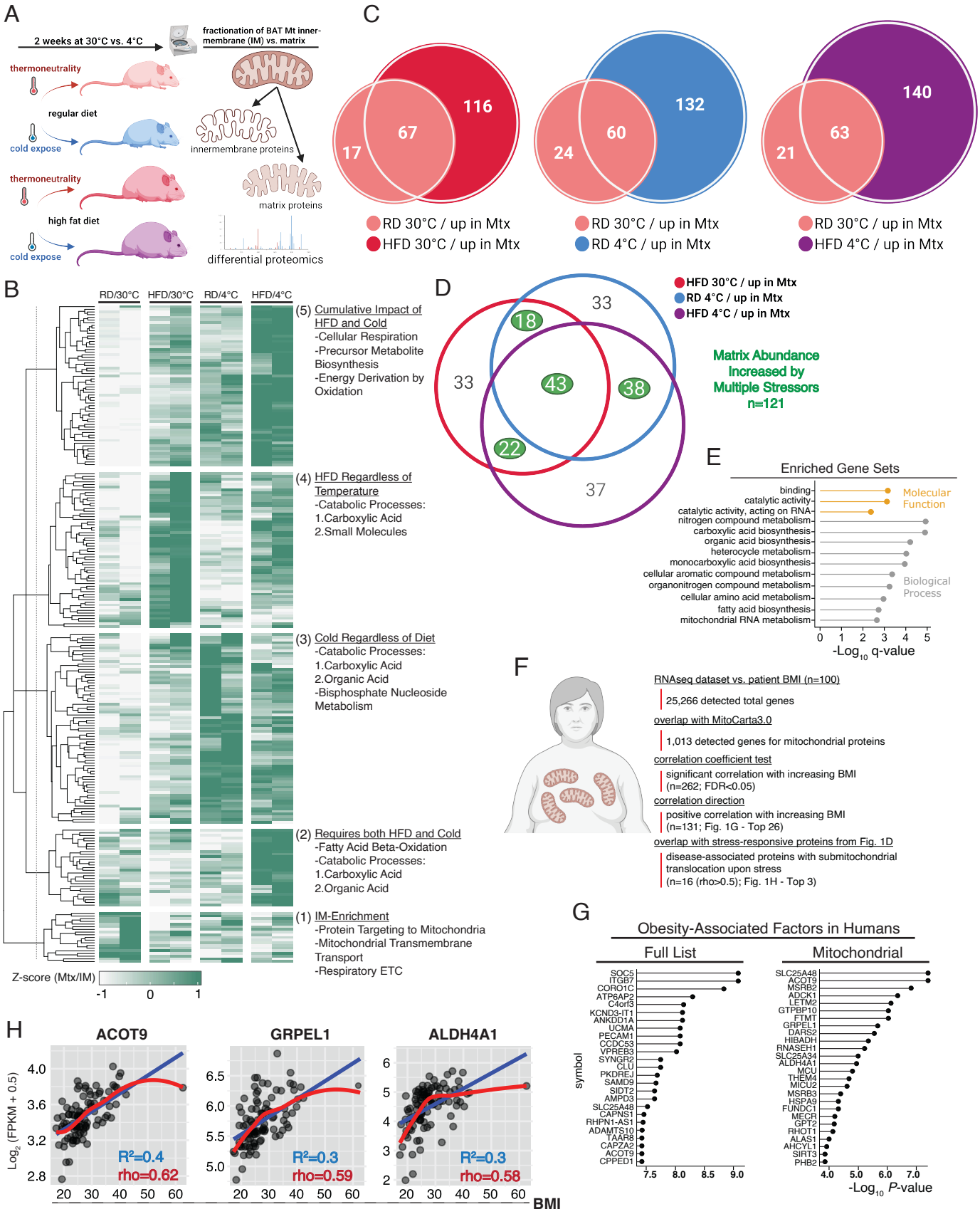
A
2 weeks at 30°C vs. 4°C
fractionation of BAT Mt inner-membrane (IM) vs. matrix
thermoneutrality
regular diet
cold expose
thermoneutrality
high fat diet
cold expose
innermembrane proteins
matrix proteins
differential proteomics
C
116
67
17
132
60
24
140
63
21
RD 30°C / up in Mtx
HFD 30°C / up in Mtx
RD 30°C / up in Mtx
RD 4°C / up in Mtx
RD 30°C / up in Mtx
HFD 4°C / up in Mtx
B
RD/30°C
HFD/30°C
RD/4°C
HFD/4°C
(5) Cumulative Impact of HFD and Cold
-Cellular Respiration
-Precursor Metabolite Biosynthesis
-Energy Derivation by Oxidation
(4) HFD Regardless of Temperature
-Catabolic Processes:
1.Carboxylic Acid
2.Small Molecules
(3) Cold Regardless of Diet
-Catabolic Processes:
1.Carboxylic Acid
2.Organic Acid
-Bisphosphate Nucleoside Metabolism
(2) Requires both HFD and Cold
-Fatty Acid Beta-Oxidation
-Catabolic Processes:
1.Carboxylic Acid
2.Organic Acid
(1) IM-Enrichment
-Protein Targeting to Mitochondria
-Mitochondrial Transmembrane Transport
-Respiratory ETC
Z-score (Mtx/IM)
-1
0
1
D
HFD 30°C / up in Mtx
RD 4°C / up in Mtx
HFD 4°C / up in Mtx
33
18
33
43
38
22
37
Matrix Abundance Increased by Multiple Stressors n=121
E
Enriched Gene Sets
binding
catalytic activity
catalytic activity, acting on RNA
nitrogen compound metabolism
carboxylic acid biosynthesis
organic acid biosynthesis
heterocycle metabolism
monocarboxylic acid biosynthesis
cellular aromatic compound metabolism
organonitrogen compound metabolism
cellular amino acid metabolism
fatty acid biosynthesis
mitochondrial RNA metabolism
Molecular Function
Biological Process
0 1 2 3 4 5
-Log10 q-value
F
RNAseq dataset vs. patient BMI (n=100)
25,266 detected total genes
overlap with MitoCarta3.0
1,013 detected genes for mitochondrial proteins
correlation coefficient test
significant correlation with increasing BMI (n=262; FDR<0.05)
correlation direction
positive correlation with increasing BMI (n=131; Fig. 1G - Top 26)
overlap with stress-responsive proteins from Fig. 1D
disease-associated proteins with submitochondrial translocation upon stress (n=16 (rho>0.5); Fig. 1H - Top 3)
G
Obesity-Associated Factors in Humans
Full List
Mitochondrial
symbol
SOC5
ITGB7
CORO1C
ATP6AP2
C4orf3
KCND3-IT1
ANKDD1A
UCMA
PECAM1
CCDC53
VPREB3
SYNGR2
CLU
PKDREJ
SAMD9
SIDT2
AMPD3
SLC25A48
CAPNS1
RHPN1-AS1
ADAMTS10
TAAR8
CAPZA2
ACOT9
CPPED1
7.5 8.0 8.5 9.0
SLC25A48
ACOT9
MSRB2
ADCK1
LETM2
GTPBP10
FTMT
GRPEL1
DARS2
HIBADH
RNASEH1
SLC25A34
ALDH4A1
MCU
THEM4
MICU2
MSRB3
HSPA9
FUNDC1
MECR
GPT2
RHOT1
ALAS1
AHCYL1
SIRT3
PHB2
4.0 5.0 6.0 7.0
-Log10 P-value
H
ACOT9
GRPEL1
ALDH4A1
Log2 (FPKM + 0.5)
4.0
3.6
3.2
2.8
R²=0.4
rho=0.62
6.5
6.0
5.5
5.0
R²=0.3
rho=0.59
6
5
4
3
2
R²=0.3
rho=0.58
20 30 40 50 60
BMI

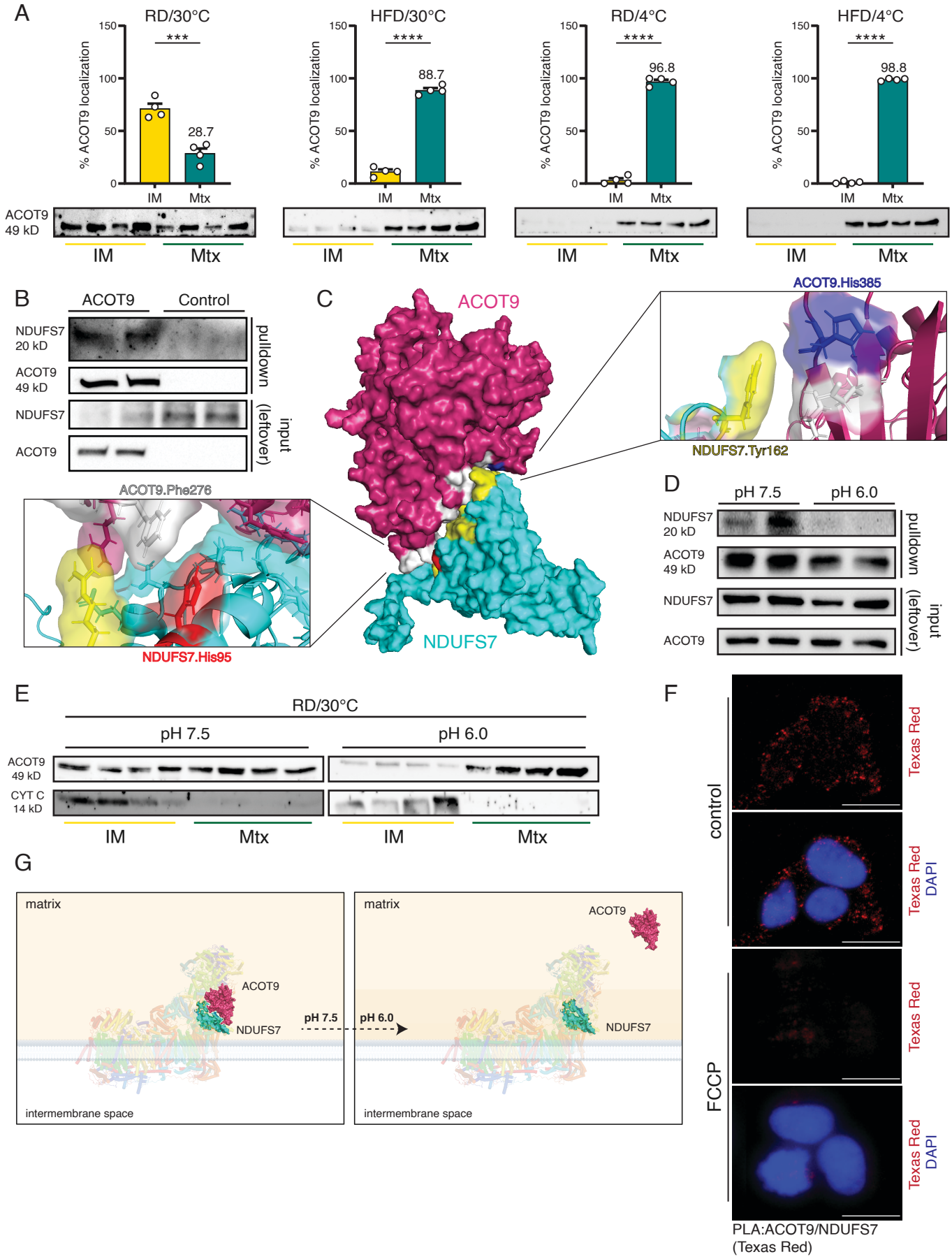
A
RD/30°C
HFD/30°C
RD/4°C
HFD/4°C
% ACOT9 localization
***
****
28.7
88.7
96.8
98.8
IM
Mtx
ACOT9
49 kD
B
ACOT9
Control
NDUFS7
20 kD
ACOT9
49 kD
NDUFS7
ACOT9
pulldown
input
(leftover)
ACOT9.Phe276
NDUFS7.His95
C
ACOT9
NDUFS7
ACOT9.His385
NDUFS7.Tyr162
D
pH 7.5
pH 6.0
NDUFS7
20 kD
ACOT9
49 kD
NDUFS7
ACOT9
pulldown
input
(leftover)
E
RD/30°C
pH 7.5
pH 6.0
ACOT9
49 kD
CYT C
14 kD
IM
Mtx
F
control
FCCP
Texas Red
Texas Red
DAPI
PLA:ACOT9/NDUFS7
(Texas Red)
G
matrix
ACOT9
NDUFS7
pH 7.5
pH 6.0
intermembrane space

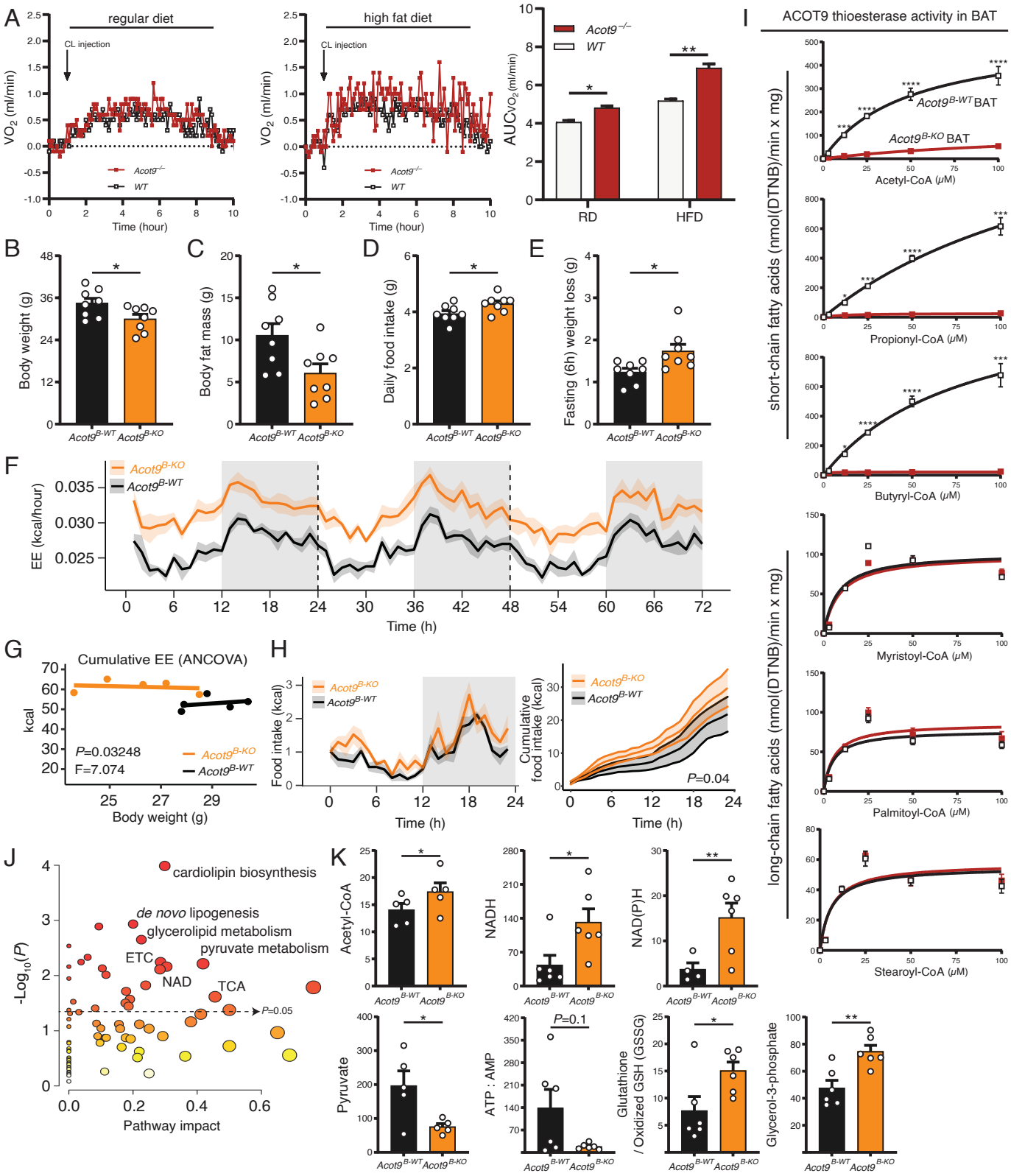
A
regular diet
high fat diet
CL injection
VO2 (ml/min)
Time (hour)
Acot9−/−
WT
AUCVO2(ml/min)
RD
HFD
I
ACOT9 thioesterase activity in BAT
Acot9B-WT BAT
Acot9B-KO BAT
short-chain fatty acids (nmol(DTNB)/min x mg)
long-chain fatty acids (nmol(DTNB)/min x mg)
Acetyl-CoA (μM)
Propionyl-CoA (μM)
Butyryl-CoA (μM)
Myristoyl-CoA (μM)
Palmitoyl-CoA (μM)
Stearoyl-CoA (μM)
B
Body weight (g)
C
Body fat mass (g)
D
Daily food intake (g)
E
Fasting (6h) weight loss (g)
Acot9B-WT
Acot9B-KO
F
EE (kcal/hour)
Time (h)
G
Cumulative EE (ANCOVA)
kcal
P=0.03248
F=7.074
Body weight (g)
H
Food intake (kcal)
Cumulative food intake (kcal)
P=0.04
J
cardiolipin biosynthesis
de novo lipogenesis
glycerolipid metabolism
pyruvate metabolism
ETC
NAD
TCA
P=0.05
-Log10(P)
Pathway impact
K
Acetyl-CoA
NADH
NAD(P)H
Pyruvate
ATP : AMP
P=0.1
Glutathione / Oxidized GSH (GSSG)
Glycerol-3-phosphate

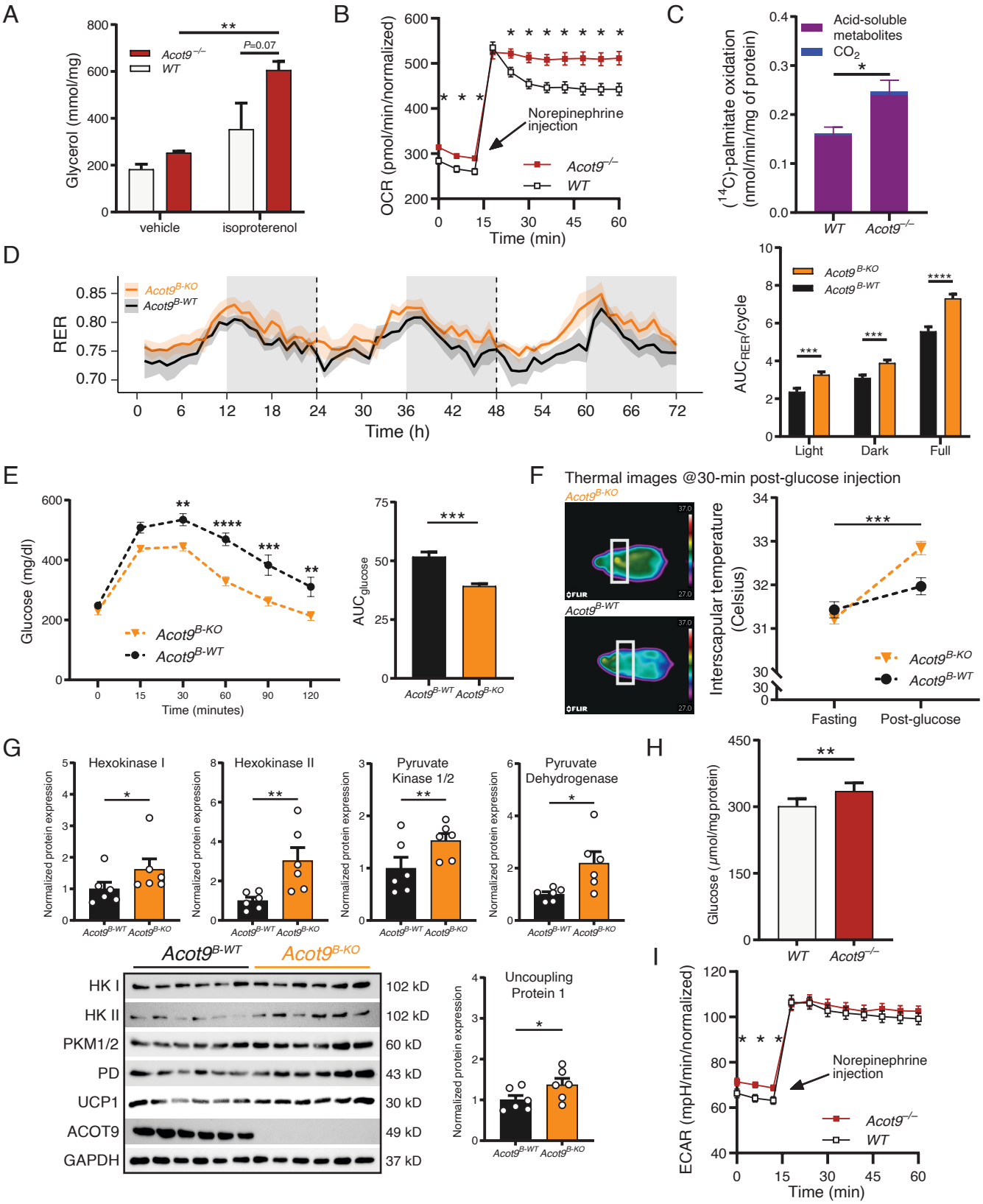
A
Glycerol (mmol/mg)
Acot9−/−
WT
P=0.07
vehicle
isoproterenol
B
OCR (pmol/min/normalized)
Norepinephrine injection
Acot9−/−
WT
Time (min)
C
Acid-soluble metabolites
CO2
(14C)-palmitate oxidation (nmol/min/mg of protein)
WT
Acot9−/−
D
RER
Acot9B-KO
Acot9B-WT
Time (h)
AUCRER/cycle
Light
Dark
Full
E
Glucose (mg/dl)
Time (minutes)
AUCglucose
F
Thermal images @30-min post-glucose injection
Interscapular temperature (Celsius)
Fasting
Post-glucose
G
Hexokinase I
Hexokinase II
Pyruvate Kinase 1/2
Pyruvate Dehydrogenase
Normalized protein expression
HK I
HK II
PKM1/2
PD
UCP1
ACOT9
GAPDH
102 kD
60 kD
43 kD
30 kD
49 kD
37 kD
Uncoupling Protein 1
H
Glucose (μmol/mg protein)
I
ECAR (mpH/min/normalized)
Norepinephrine injection
Time (min)